ENGINEERING

Fully printed and self-compensated bioresorbable electrochemical devices based on galvanic coupling for continuous glucose monitoring

Jiameng Li[1], Jiayin Liu[1], Ziyue Wu[1], Xue Shang[1], Ya Li[1], Wenxing Huo[1], Xian Huang[1,2]*

Real-time glucose monitoring conventionally involves non-bioresorbable semi-implantable glucose sensors, causing infection and pain during removal. Despite bioresorbable electronics serves as excellent alternatives, the bioresorbable sensor dissolves in aqueous environments with interferential biomolecules. Here, the theories to achieve stable electrode potential and accurate electrochemical detection using bioresorbable materials have been proposed, resulting in a fully printed bioresorbable electrochemical device. The adverse effect caused by material degradation has been overcome by a molybdenum-tungsten reference electrode that offers stable potential through galvanic-coupling and self-compensation modules. In vitro and in vivo glucose monitoring has been conducted for 7 and 5 days, respectively, followed by full degradation within 2 months. The device offers a glucose detection range of 0 to 25 millimolars and a sensitivity of 0.2458 microamperes per millimolar with anti-interference capability and biocompatibility, indicating the possibility of mass manufacturing high-performance bioresorbable electrochemical devices using printing and low-temperature water-sintering techniques. The mechanisms may be implemented developing more comprehensive bioresorbable sensors for chronic diseases.

INTRODUCTION

Diabetes (*1*–*3*) is currently affecting more than 425 million people globally (*4*, *5*). Despite that discrete finger pricks are still the most prevalent methods to conduct glucose monitoring, novel continuous glucose monitoring (CGM) technologies have been developed to detect glucose in various body fluids, such as blood (*6*–*8*), interstitial fluid (*9*–*11*), urine (*12*, *13*), and sweat (*14*, *15*), through electrochemical sensing. Among them, glucose monitoring through interstitial fluids is one of the most effective alternatives to reflect the actual blood sugar levels due to highly correlative compositions in the interstitial fluid and the blood. Thus, several renowned commercial products based on semi-implantable rigid glucose sensors have been widely available for patients with type I and type II diabetes (*16*–*18*). However, the majority of commercial real-time glucose monitors, which typically use non-bioresorbable materials with a life span ranging from 7 to 14 days may induce the potential risk of infection, local thrombosis, and tissue damage due to the frequent insertion and removal of the probes (table S1).

Efforts to eliminate the need to retrieve implanted devices and minimize associated inflammatory responses have led to the development of bioresorbable electronics or transient electronics, which last for a certain period and then disappear through material hydrolysis, enzyme-assisted degradation, and tissue absorption. These types of devices offer diverse applications such as brain pressure monitoring (*19*), tendon strain recording (*20*), and cortical electrical stimulation (*21*–*23*). Despite that these bioresorbable devices have exhibited desirable performance and capability to compete with their non-transient counterparts in physical signal sensing, the creation of fully bioresorbable devices for chemical sensing remains extremely challenging. The need to directly expose the sensors to aqueous environments with all kinds of interferential biomolecules conflicts with the requirement to protect the devices from liquids and ions. Some electrochemical sensors that have been developed to detect biomolecules such as nitric oxide (*24*), glucose (*25*), and dopamine (*26*) are only partially bioresorbable, as the use of inert electrode materials such as gold (Au), carbon (C), and silver/silver chloride (Ag/AgCl) is still unavoidable. Fully bioresorbable electrochemical sensors have seldom been achieved, and their mechanisms and selection approaches for various electrode materials have not been systematically explored.

Here, we explore mechanisms to achieve stable electrode potential and accurate electrochemical detection based on the galvanic coupling of bioresorbable materials and develop a fully printable bioresorbable electrochemical device with self-compensation capability for CGM. The glucose sensor contains a zinc (Zn) working electrode (WE), a molybdenum (Mo) counter electrode (CE), and a Mo-tungsten (Mo-W) reference electrode (RE). In addition, the negative effect of material degradation can be compensated by the self-compensation modules that include a Zn sacrificial electrode (SE), a temperature sensor, and a dissolved oxygen (DO) sensor. Real-time monitoring of glucose has been conducted both in vitro and in vivo for up to 7 and 5 days, respectively, demonstrating accurate glucose sensing capability with a wide range of 0 to 25 mM and a desired sensitivity of 0.2458 μA/mM that even outweighs some conventional glucose sensors. Biocompatibility assessments revealed no obvious adverse effects or accumulation of foreign materials at implantation sites and in major organs. The device reveals the possibility to use screen printing and low-temperature water-sintering techniques to achieve scalable and mass-manufacturable bioresorbable electrochemical devices. It is one of the first fully bioresorbable electrochemical systems that can realize implantable glucose monitoring with a low risk of tissue irritation and infection.

[1]Department of Biomedical Engineering, Tianjin University, 92 Weijin Road, Tianjin 300072, China. [2]Institute of Wearable Technology and Bioelectronics, Qiantang Science and Technology Innovation Center, 1002 23rd Street, Hangzhou 310018, China.
*Corresponding author Email: huangxian@tju.edu.cn

The proposed theories and mechanisms may lead to the development of comprehensive bioresorbable sensing systems and diverse sensors that may revolutionize the diagnosis and treatment of chronic diseases.

RESULTS

Overall design of the system

The concept of the fully printed bioresorbable electrochemical device for glucose monitoring in subcutaneous tissues has been shown in Fig. 1A. The bioresorbable device contains a glucose sensor, a DO sensor, and a temperature sensor fabricated on a poly(lactic-co-glycolic acid) (PLGA) substrate and connects with a wireless control circuit made of flexible printed circuit boards. The sensors and electrodes in the device are based on Zn paste, Mo paste, and Mo-W paste that are screen-printed and water-sintered to yield conductive patterns and offer stable performance over the entire sensing period. The detailed water-sintered mechanism and method were presented in the Supplementary Materials. A detailed mechanism and a workflow to achieve stable glucose sensing using the device have been shown in Fig. 1B and fig. S1. Briefly, the Zn electrodes that were coated with glucose oxidase (GO_x) and the catalase, respectively, serve as the WEs for the glucose sensor and the DO sensor to measure the glucose and the DO in the interstitial fluid simultaneously. Moreover, the RE and CE were both connected to an external voltage of 1.75 V, while the WE and the SE were connected to an external voltage of 1.65 V. As a result, a fixed bias voltage of 0.1 V was established between the RE and the WE/SE within the system. To maintain this stable potential, the circuit between the RE and the WE/SE electrodes remained open to prevent current flow. This configuration ensured the stability of the RE potential, serving as a reliable reference point. Instead, a closed circuit was formed between the CE and the WE/SE, creating a voltage difference of 0.1 V to measure the reaction currents. Meanwhile, a Zn SE is deliberately used to detect the current changes during its degradation process under the external voltage. The relatively stable levels of DO in body fluids offer excellent references to overcome the drift in glucose signal caused by electrode degradation. The drift in the DO sensor can then be considered purely caused by the degradation of the DO sensor, which has a similar degradation rate as the glucose sensor. The RE, which is the essential component of the glucose sensor and the DO sensor, is made of the composite of Mo and W microparticles (MPs) that generate potential differences due to their electrode potentials. Collective characteristics of the composite can manifest as a stable electrode potential influenced by the ratios of the overall surface area of two kinds of MPs. In addition, the temperature sensor measures the environmental temperature for real-time correction of temperature-dependent electrochemical sensing results. Ultimately, the corrected glucose concentration is calculated on the basis of a correction model described in detail in the Supplementary Materials.

A typical bioresorbable electrochemical device 4 mm by 1.5 cm by 260 μm in dimension (Fig. 1C) can be deformed to fit implantation sites with minimal damage to dorsal subcutaneous tissue, while a wireless circuit whose schematic diagrams have been shown in Fig. 1D and fig. S2 can be easily affixed to the dorsal surface. The resulting system is only 3.65 g in weight (fig. S3), allowing the free moving of a rat and minimum interference to its daily life (Fig. 1E). After encapsulating the device with a PLGA film and submerging the device in phosphate-buffered saline (PBS) (pH 7.4) solution at room temperature, the device gradually disintegrated into small fragments within 2 months (Fig. 1F).

Characterization of the electrochemical electrodes

As the most important components to ensure the success of the device, the construction and mechanisms of different REs have been investigated. Figure 2A illustrates the mechanism of a galvanic couple RE, which is formed by two metal particles with varying standard electrode potentials. In a galvanic couple with a potential difference of ΔE, the more noble metal that undergoes cathodic polarization acts as the cathode (cat), while the more active metal serves as the anode (an). Since the galvanic couple potential (E_p) is determined by the point where the total anodic current is equal to the total cathodic current, the area of each coupling half affects the couple potential. This area effect shifts the anodic currents to higher values at the same potentials, decreasing E_p by lowering the point where the total cathodic and anodic currents intersect (*27*). By adopting this approach, the area of each half of the couple can be tuned to achieve predictable performance such as durability and corrosion resistance of the galvanic couple REs. Different from conventional REs that generally use metal salts that exhibit poor degradability, galvanic couple REs based on two soluble metals with different activities have tremendous potential for bioresorbable electrochemical sensors (*28*).

Bioresorbable pastes that may be used as RE based on nanoparticles (NPs) and MPs of Zn, Mo, and W with different mixing ratios were compared. The exact specifications of different paste compositions have been shown in table S2. Optimizing the particle size and the proportion of Mo and W particles in pastes is crucial to achieving high electrical conductivity. All examined pastes containing Mo and W particles have conductivities ranging from 1000 to 2500 S/m after being water-sintered for 30 to 40 min at room temperature (Fig. 2B). The paste that comprises Mo and W particles with a diameter of 1 μm and weight ratios both at 25% has a conductivity of 2328.98 S/m, which is much higher than that of Mo-W pastes with the same weight ratios but different particle sizes of 50 nm and 5 μm. The REs should have sufficient conductivity to facilitate effective current conduction in the electrolyte environment, while specific threshold information regarding conductivity requirements remains unclear. Scanning electron microscopy (SEM) images presented in Fig. 2 (C and D) reveal distinct differences in the pastes before and after sintering. The superior conductivity of the pastes consisting of 1 μm of Mo and W particles may be attributed to the polyhedral particle shapes, which facilitate physical contact among particles over large surface areas while maintaining small contact resistance. In contrast, diminish particle sizes may lead to increased contact resistance, and enlarged particle sizes may result in a larger porosity and reduced chances of physical contact (fig. S4). In comparison, the electrode with Zn-W and Zn-Mo pastes exhibits significantly higher conductivities of 23668.62 and 22287.78 S/m, respectively (fig. S5). This outcome may be attributed to the reactivity difference between Zn and Mo as well as Zn and W, resulting in intense ion diffusion and redeposition during the water-sintering process.

The stability and stable electrode potentials of REs are also crucial factors for accurate electrochemical detection. Thus, REs with different compositions were immersed into the 1× PBS solution and measured continuously for 8 hours against a commercial

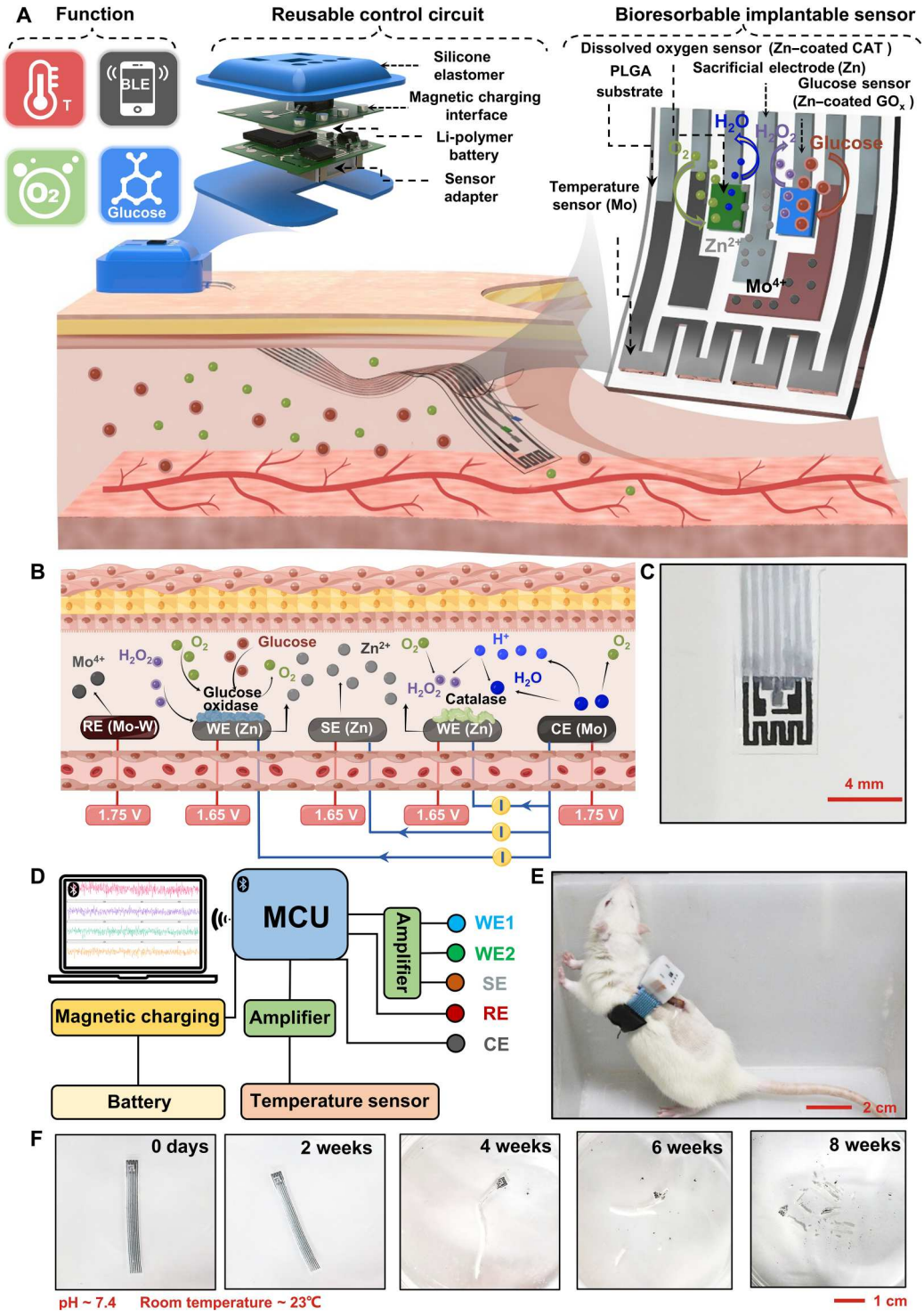

Fig. 1. Concepts and demonstration of the bioresorbable electrochemical device. (**A**) Schematic illustration of the bioresorbable electrochemical device. (**B**) The mechanism of the three-electrode system for glucose detection with an additional SE and a DO sensor. (**C**) Representative image of the sensor. (**D**) System-level diagram showing the electrical components of the system; MCU, Microcontroller Unit. (**E**) Image of a rat that is wearing the monitoring system on the dorsal. (**F**) Dissolution processes of the bioresorbable electrochemical device after immersing in phosphate-buffered saline (PBS) solution. PLGA, poly(lactic-co-glycolic acid); cat, catalase; GO_x, glucose oxidase.

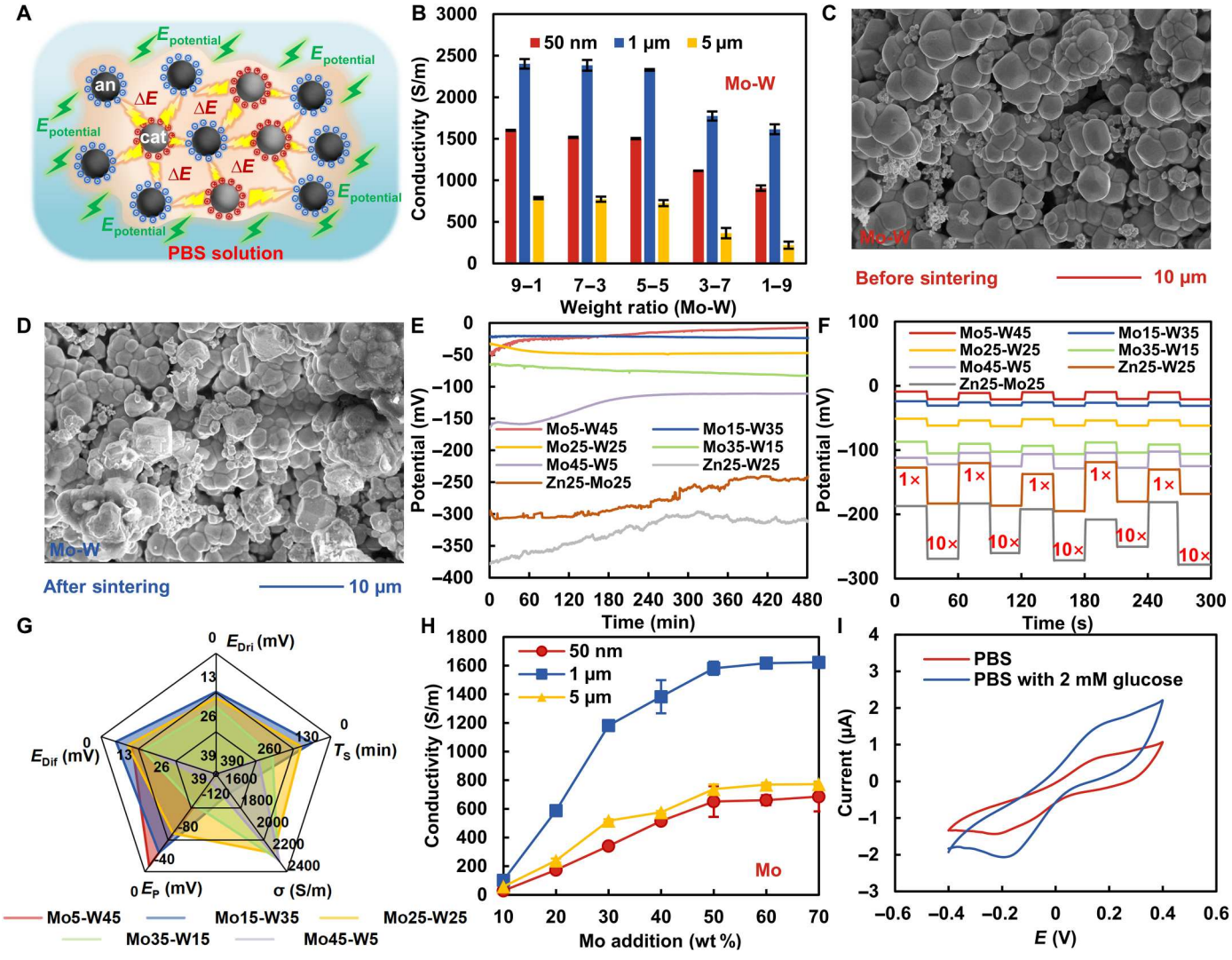

Fig. 2. Characterizations of the bioresorbable electrochemical device. (**A**) A schematic of the RE mechanism. (**B**) Conductivity of Mo-W pastes with different weight ratios and particle sizes. Surface morphology of bioresorbable patterns printed with 25 wt % of Mo MPs (1 μm) and 25 wt % of W MPs (1 μm) before (**C**) and after (**D**) sintering. (**E**) Stability test of different REs in 1× PBS solution for 8 hours against a commercial Ag/AgCl RE. (**F**) Potential time graph of repeatability measurements for different REs in 1× and 10× PBS solution. (**G**) Radar plots of the Mo-W REs with different ratios based on five parameters. Stable electrode potential (E_p): the constant potential that can be achieved by the RE under specific experimental conditions. Conductivity (σ): the ability of the RE to conduct electricity in the given electrolyte environment. Time to reach a stable potential (T_S): the duration required for the RE to achieve the E_p. Potential drift (E_{Dri}): the continuous alteration in potential exhibited by the RE throughout the measurement. Repeatability difference (E_{Dif}): the disparity in repeatability observed among the RE potentials derived from repeated measurements. (**H**) Conductivity of the bioresorbable pastes with different Mo particle sizes and concentrations. (**I**) Cyclic voltammetry curves in pure PBS solution and PBS solution containing 2 mM glucose measured by the bioresorbable glucose sensor.

Ag/AgCl RE to investigate their stability and potential difference (Fig. 2E and table S2). Despite the superior conductivity of Zn-W and Zn-Mo REs, their potentials decay by 80.73 and 76.26 mV, respectively, failing to meet the RE stability requirements of 30 mV (*29*). The large potential decay and the difficulty in maintaining the steady state may be due to the large potential difference between Zn and W as well as Zn and Mo, resulting in constant corrosion of the Zn particles. All REs made of Mo-W pastes exhibit a stable potential (E_p) after fluctuations during which the two metals are polarized into a combined potential couple. The duration of the fluctuation process may be determined by the total surface area of Mo and W MPs (fig. S6). Among different ratios of Mo and W, the Mo15-W35 RE in which the numbers 15 and 35 next to the elements denote the weight ratios exhibits the best stability with a minimized time to reach a stable potential (E_p) and a minimized potential drift (E_{Dri}) likely because the ratio of total surface area between W and Mo in this RE is the closest to 1. Reducing the time to reach a stable potential (T_s) can enhance testing efficiency and mitigate potential experimental errors as electrode potentials may exhibit notable fluctuations before stabilizing. Moreover, the total surface area ratio of W and Mo is also logarithmically related to the E_p of the REs with a correlation coefficient of 0.96 (fig. S7). While the requirement for the E_p may not be strictly imposed on the REs, the crucial aspect lies in ensuring a stable

reference potential to attribute changes in current during measurements majorly to the concentrations of analytes on the WEs. In addition, the repeatability difference (E_{Dif}) of the REs was also determined by repeatedly measuring the E_p in 1× and 10× PBS solutions, respectively. The potential changes of Mo15-W35 and Mo25-W25 REs are 5.23 and 9.21 mV, lower than the threshold value of 10 mV which represents the good quality of typical RE (Fig. 2F) (*29*). Furthermore, stability tests of the REs made of Mo15-W35 and Mo25-W25 have been conducted for 1 week. Figure S8 has shown that the potential of the Mo15-W35 and the Mo25-W25 REs decay 12.11 and 20.46 mV, respectively, after 7 days, comparing smaller than the 30-mV threshold (*29*). These findings confirm the exceptional stability of both compositions and demonstrate their potential use in practical applications. According to a radar chart in Fig. 2G, Mo25-W25 may be the optimal formula to allow a high-performance bioresorbable RE by comprehensively considering five parameters including E_p, σ, T_S, E_{Dri}, and E_{Dif}.

The difference in electrochemical stability among Zn-Mo, Zn-W, and Mo-W electrodes has been studied using finite element analysis incorporating electrochemical and transformed geometrical physical fields. Since the internal change of the electrode is a spontaneous process, the boundary condition of the electrode surface with an external potential of 0 V was applied in the model. In addition, a simplified model existed within an electrically neutral solution environment with a size of $2 \times 2\ \mu m^2$ has been built (fig. S9). Moreover, the top and bottom curved surfaces represent the interfaces between the electrolyte and the more active metal MPs with a diameter of 1 μm, while the left and right curved surfaces represent the interfaces between the electrolyte and the less active metal MPs with a diameter of 1 μm. A larger number of Zn^{2+} were released from the Zn anode since the increase in the area of the cathode and decrease in the area of the anode could be observed in the Zn-W and Zn-Mo models (fig. S9, A and B). However, almost no change in Mo ion concentrations and boundary morphology can be observed in the Mo-W model (fig. S9C). The anode thicknesses of the Zn-W and Zn-Mo models corresponding to the upper curved surface decreased by 21.21 and 9.85 nm, respectively, within 1 ms, while the Mo-W model only decreased by 0.04 nm (fig. S9, D and E), indicating a much slower dissolution rate of the Mo-W electrode. These simulation results show that the Mo-W electrode has a much slower dissolution rate than other combinations of soluble metals, suggesting a great potential to act as a bioresorbable RE.

The characteristics of the soluble metals as CE and WE materials have also been investigated. Despite that pure Mo may not be a good candidate for RE, it has demonstrated potential as dissolvable interconnects and CEs (*30*, *31*). Conductivities of Mo pastes with varying particle sizes were compared, revealing that Mo particles with diameters of 1 μm exhibited higher conductivity than those with smaller (~50 nm) or larger (~5 μm) diameters (Fig. 2H). The paste with 50 wt % Mo of 1-μm diameter may be the optimal formula to allow high-performance bioresorbable patterns. The stability of the Mo electrode was investigated in 1× PBS solution against a commercial Ag/AgCl RE, demonstrating stable potential at −0.18 V with a slight fluctuation of 4 mV during continuous testing for 8 hours (fig. S10). Moreover, further investigations were conducted to demonstrate the stability of the W and the Zn electrodes in 1× PBS solution against a commercial Ag/AgCl RE. The results have shown that the W and the Zn electrodes have potential at −0.04 and −0.81 V with a fluctuation of 3 and 37 mV, respectively, during continuous tests for 8 hours (fig. S11). Despite slightly higher fluctuations observed in the Mo electrode compared to the W electrode (with a difference of only 1 mV), the high conductivity of the Mo paste has led to its selection as the CE throughout the following experiments (fig. S12). Meanwhile, the WE acts a critical role in measuring the analyte concentrations and therefore needs to have excellent conductivity to ensure low-loss current flow. Therefore, the water-sintered Zn electrodes that have a higher conductivity of 71362.21 S/m than Mo and W electrodes were chosen as the WEs (fig. S12). Furthermore, a Zn SE is purposed to monitor the current variation throughout the degradation process under the external voltage. The response currents of the WE and the SE were measured in a PBS solution containing 2 mM glucose for 8 hours. The WE coated with the GO_x on its surface exhibited a similar decaying trend to the SE with a slope of about −0.009 μA/h (fig. S13). The difference in the current of the WE and the SE is 2.92 μA at the 2 mM glucose concentration over the entire measurement period, indicating the necessity to integrate the SE in the device for compensating the effect of degradation in all WEs under the external voltage. Moreover, the performance of the electrochemical electrode configuration comprising Zn, Mo, and Mo-W electrodes was investigated in the presence of glucose using cyclic voltammetry (CV). CV curves obtained in PBS solution and 2 mM glucose solution ranging from −0.4 to 0.4 V indicate discernible peaks corresponding to the oxidation and reduction of H_2O_2 at −0.18 and 0.17 V, respectively (Fig. 2I). These results demonstrate the competence of the Zn/Mo/Mo-W three-electrode configuration for electrochemical analysis, as it enables precise identification of the redox behavior of glucose in the solution.

In vitro measurement of the bioresorbable electrochemical device

The sensing capabilities of the glucose sensor in the bioresorbable electrochemical device were first characterized at a temperature of 37°C. The glucose sensor demonstrates a linear response at physiologically relevant concentrations from 0 to 25 mM with a sensitivity of 0.2458 μA/mM as shown in Fig. 3A and fig. S14. Detailed test results for glucose concentrations below the 1 mM interval can be found in fig. S15. Note that the lowest detectable glucose concentration and the minimum glucose concentration gradient are both 0.1 mM, thereby implying the lowest detection limit and the resolution of 0.1 mM for the glucose sensor. The sensing range and sensitivity of this glucose sensor are higher than that of traditional glucose sensors, indicating the superiority of the bioresorbable glucose sensor present in this work (fig. S16). The selectivity and specificity of the glucose sensor were comprehensively assessed through rigorous investigations involving common interfering substances in biological systems including Ca^{2+}, Na^+, uric acid (UA), and ascorbic acid (AA). Figure 3B demonstrates the ability of the sensor to accurately measure glucose in the presence of potential interferences. To quantitatively demonstrate the specificity of the glucose sensor in glucose detection, further analysis of the glucose sensor was shown in fig. S17. With the addition of potential interfering chemicals with concentrations of 2 mM, the sensor′s response to glucose is at least 88% higher than other interferences. The physiological concentrations of various essential ions and metabolites have been provided in table S3. Notably, a concentration of 2 mM

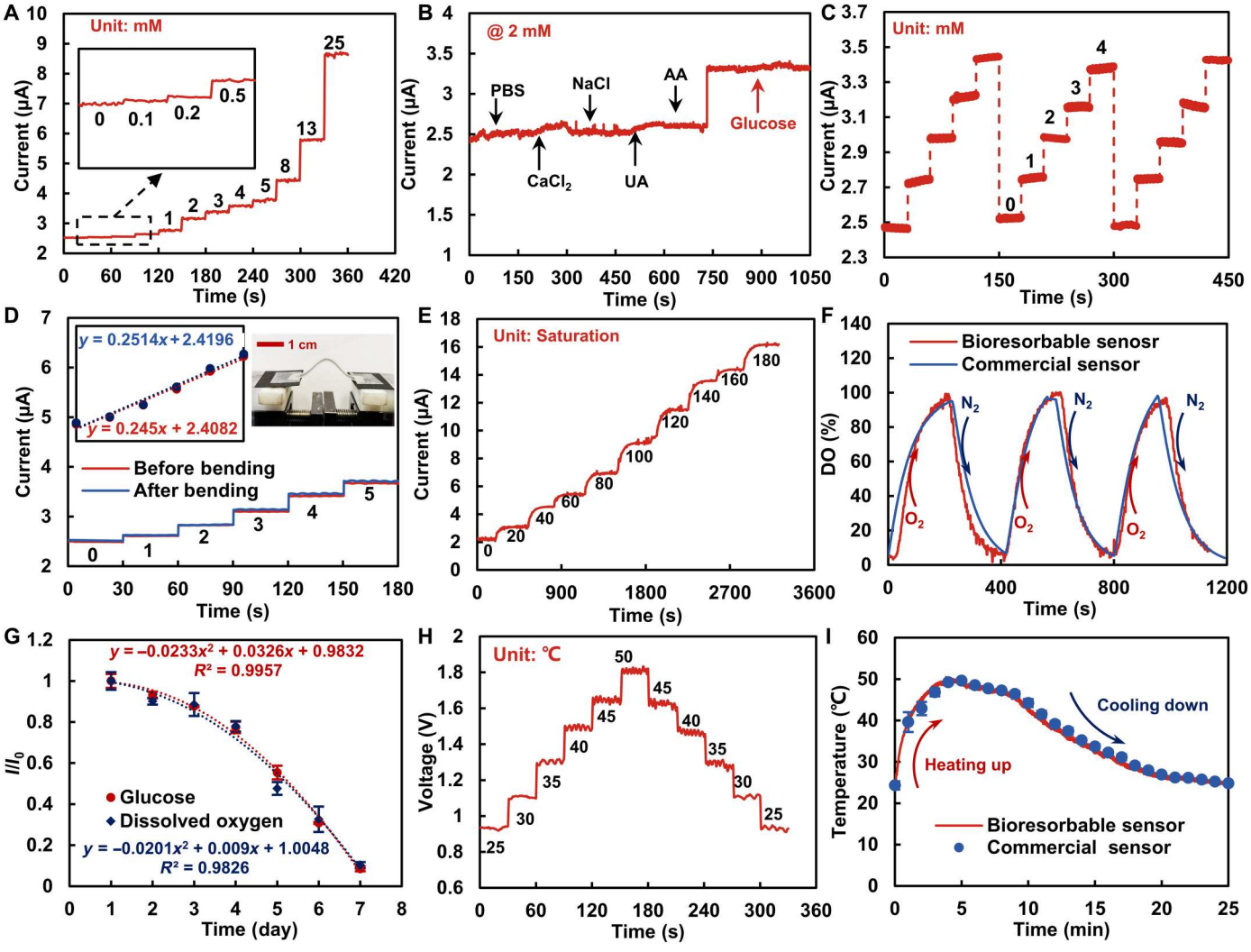

Fig. 3. In vitro characterization of the bioresorbable electrochemical device. (**A**) Time-dependent current response of the glucose sensor at different glucose concentrations from 0 to 25 mM in PBS solution at 37°C. Selectivity (**B**), reversibility (**C**), and mechanical robustness (**D**) of the bioresorbable electrochemical device. (**E**) Time-dependent current response of the DO sensor at different DO saturation from 0 to 180%. (**F**) Real-time responses of the DO sensor from 0 to 100% DO saturation in comparison with a commercial DO sensor. (**G**) Changes in the current response of the glucose sensor and the DO sensor in the bioresorbable device after being immersed in 5 mM glucose solution with a DO level of 90% for 1 week. (**H**) Temperature changes measured by the temperature sensor from 25° to 50°C. (**I**) Real-time responses of the temperature sensor in comparison with a commercial standard thermometer.

apparently exceeds the levels of Ca^{2+}, UA, and AA in the subcutaneous tissue. To quantify the influence of excessive Na^+ on glucose detection, 150 mM Na^+ was added to a PBS solution followed by the addition of 2 mM glucose; an unconspicuous change in the measured signal can be observed in fig. S18 after the addition of the Na^+. These results suggest that the sensor has outstanding specificity to glucose. In addition, the forward potentiometric measurements of the sensor show stable and fast responses to varying glucose concentrations, with a 1.67% relative SD of sensitivity (Fig. 3C and fig. S19). The mechanical robustness of the bioresorbable sensor was demonstrated by a stable current response after repeated bending. The current changes from 0.245 to 0.2514 μA/mM with only a 2.61% decrease after 5000 times of bending to a curvature radius of 3.5 mm (Fig. 3D). A more detailed comparison of major features between different glucose sensors has been provided in table S4 (*25*, *32*–*48*), and the bioresorbable glucose sensor has a detection limit of 0.1 mM, which is compared much better than many conventional glucose sensors whose WEs do not contain nanostructures. Considering the typical fasting blood glucose concentration is 3.9 mM, the detection limit of the bioresorbable glucose sensor should be sufficient to meet daily and clinical needs.

The DO sensor and temperature sensor have been characterized, and their capabilities to calibrate glucose sensing results have also been demonstrated. The linear current response to different DO saturation from 0 to 180% has been observed in Fig. 3E. The measured results exhibit a linear response up to approximately 180% of DO saturation with a sensitivity of 0.0812 μA/% and a correlation coefficient (R^2) of 0.98 (fig. S20). When compared with a commercial DO sensor by repeatedly purging O_2 and N_2 into deionized (DI) water, the bioresorbable DO sensor exhibited a nearly identical

response as the commercial sensor (Fig. 3F). To construct a real-time glucose calibration model based on DO measurement, both the glucose sensor and the DO sensor were tested under a glucose level of 5 mM and a DO level of 90% for a week. The current response of glucose and DO concentrations decays consistently by following a similar trend (Fig. 3G). In addition, the measurement sensitivities stayed almost constant at 0.26 and 0.08 μA/mM for the glucose sensor and the DO sensor, respectively, over the first 5 days, and then gradually increased to 1.65 and 1.92 times that of the initial state on the seventh day (fig. S21). The increased sensitivity over time may be attributed to the dissolution of the WE, resulting in changes in the morphology of the surface of the electrode, which potentially amplified the specific surface area of the WE (fig. S22). The temperature dependence of device performance was also investigated to refine the temperature correction factor. The linear current response to different glucose concentrations and DO saturation at varied temperatures has been shown in fig. S23. The baseline currents show a linearly increasing tendency as the temperature increases, possibly caused by the resistance change of the device under temperature variation because of the thermal resistance effect of the electrodes (fig. S24). Both results indicate an excellent correlation between the signal measured by the two sensors, suggesting the promising potential to use DO levels to compensate for glucose sensing results. Furthermore, the bioresorbable temperature sensor features a resistance temperature coefficient of 0.16% per degree Celsius and a sensitivity of 17.5 mV per degree Celsius at a temperature range between 25° and 50°C (Fig. 3H and fig. S25). Note that the measurement sensitivity of the temperature sensor remained stable at 17.5 mV per degree Celsius with a fluctuation of 0.0003 mV per degree Celsius throughout the entire 7-day period (fig. S26). Correspondingly, the SEM images of the Mo temperature sensor have indicated minimum changes in the surface morphology before and after the 7-day measurement period (fig. S27). The comparison of a Pt-based commercial sensor and the bioresorbable temperature sensor has indicated excellent consistency between these two sensors (Fig. 3I). The above experiments have shown that the device has good accuracy in glucose, DO, and temperature monitoring, allowing the establishment of a precise calibration model based on the DO concentration and the temperature.

Bioresorption and biocompatibility of the bioresorbable electrochemical device

To investigate the biocompatibility of the bioresorbable device, the device was first coincubated with 929 clones of mouse connective tissue L cell line (L-929) to examine its cytotoxicity. Less than 1% noticeable cell necrosis can be observed in the fluorescent images obtained by Calcein-AM/propidium iodide (PI) double-stain assay (Fig. 4A). The influence of the bioresorbable device on cell proliferation was further explored using the Cell Counting Kit-8 (CCK-8) assay. Cell viability for the bioresorbable device and the control group is 96.65, 93.39, 92.59, and 97.28, 99.09, 95.01% for 24, 48, and 72 hours, respectively (Fig. 4B), meeting the required 70% cell viability as recommended by USP (ISO 10993-10995).

In vivo studies were conducted by implanting the device into the subcutaneous tissue of rats for 8 weeks. Results have shown that the implanted portion of the device became encapsulated by a fibrous capsule and underwent gradual degradation over time (Fig. 4C). In addition, the device located at the incision junction was observed to undergo gradual biosorption and breakage by the dorsal skin after 2 weeks, and the on-skin portion of the device detached after 4 weeks (Fig. 4D). Then, the surgical incision healed gradually over the next 4 weeks. The experimental and control groups exhibited similar trends in body weight, indicating no adverse effects from the implantation (Fig. 4E). Furthermore, the health conditions of the rats were obtained through complete blood counts and blood chemistry tests. The independent samples *t* test, with a significance level of $P > 0.05$, shows no significant differences between the experimental and control groups in the average counts of white blood cells, red blood cells, platelets, lymphocytes, neutrophilic granulocytes, and levels of hemoglobin over an 8-week study period (Fig. 4F). Enzymes and electrolytes that serve as important indicators in the blood for organ-specific diseases also fell within the confidence intervals of control values, indicating the absence of disorders in various organs (Fig. 4G). For instance, alanine aminotransferase, aspartate aminotransferase, urea nitrogen, and creatinine levels were all within the normal range between 20.28 and 45.71 U/liter, 85.62 and 196.98 U/liter, 2.91 and 7.45 mM, as well as 20.39 and 74.91 μM, respectively, suggesting the absence of any liver, kidney, and spleen disorders, and overall good health. Histopathological examination of tissues harvested from the control rat and the rat implanted with the bioresorbable electrochemical device for 8 weeks reveals no signs of inflammation, tissue necrosis, ischemia, or any other histological abnormalities (Fig. 4H and fig. S28). Note that the white area observed in the control group of the myocardial samples and the device group of the liver samples corresponds to the myocardial tissue gap and the central vein, respectively. The slight differences in color shades and cellular areas on the stained images are mainly due to differences in sampling batches, section thickness, and staining batches. The absence of any observable deteriorated effects on major organs and daily behavior following device implantation indicates its excellent biocompatibility for long-term monitoring. Thus, hematoxylin and eosin (H&E) staining, complete blood count, and blood chemistry tests complement each other in terms of results, providing a complete image and quantitative demonstration of the biocompatibility of the bioresorbable electrochemical devices.

Real-time in vivo glucose monitoring in living mammals

Real-time physiological monitoring of oral glucose tolerance test (OGTT) experiments was conducted on rats that had fasted for 24 hours. A 5% glucose solution was instilled in the proximal jejunum of early rats on the first, third, and fifth days, respectively (Fig. 5A). On the first day, the current response of the glucose sensor increased steadily from 4.36 to 5.21 μA corresponding to glucose concentration changed from 5.95 to 9.15 mM for the first 35 min. Subsequently, the current response fell to 4.44 μA, corresponding to the glucose concentration decreasing to 6.44 mM over the next 90 min. The fluctuations in glucose concentration are consistent with the discrete measurement results of a commercial glucometer and compatible with the normal response of healthy mice (Fig. 5B). The current response of the OGTT attenuated by 72.76 and 34.91% on the third and fifth days, respectively. Concurrently, stable DO concentrations and temperature in the rat subcutaneous tissues have been correlated with the decayed current in the DO sensor (Fig. 5, C and D), allowing the calculation of the decay rate of the current (I_D/I_{D0}) that can be used to correct glucose concentration according to eq. S12 in the Supplementary Materials.

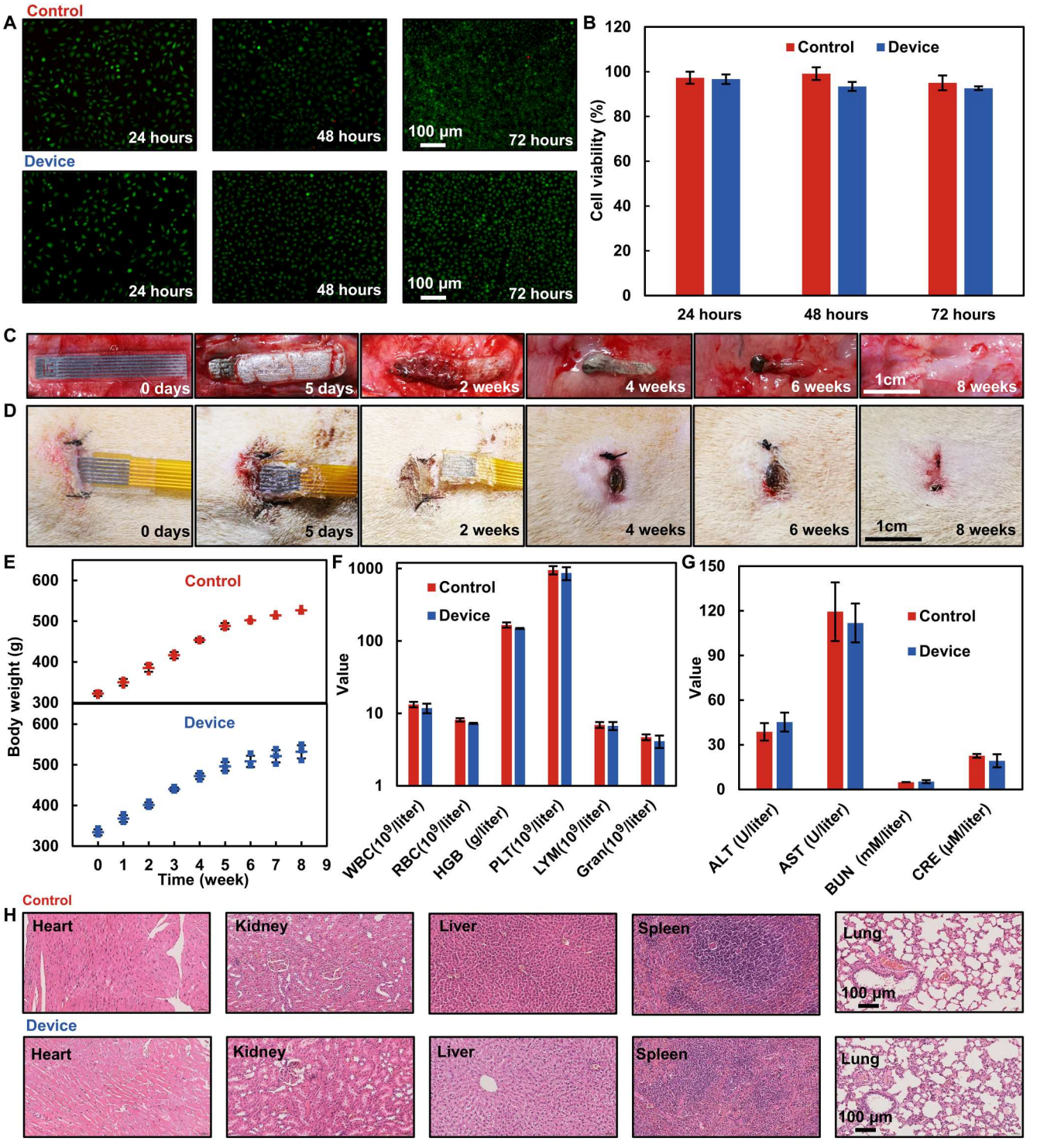

Fig. 4. In vitro and in vivo biocompatibility evaluations. (**A**) Fluorescent images of L-929 cells cultured on the bioresorbable electrochemical device for 24, 48, and 72 hours with calcein-AM/PI staining. Green (calcein-AM) for live cells and red (PI) for dead cells. (**B**) Cell viability of L-929 cells using Cell Counting Kit-8 assay after 24, 48, and 72 hours. (**C**) Images of the degradation process of the bioresorbable electrochemical device implanted in the subcutaneous tissue over 8 weeks. (**D**) Images of the degradation process of the external interconnect and wound healing process over 8 weeks. (**E**) Changes in body weight for control and experimental groups measured weekly for 8 weeks. (**F**) Results of the blood routine tests for the rats. (**G**) Results of the blood biochemistry tests for the rats. Control data are collected from three rats acquired from one batch for 8 weeks. (**H**) Histology images of the heart, kidney, liver, spleen, and lung, stained with hematoxylin and eosin of the control and experimental groups after 8 weeks. Biologically independent rat (A) to (H): control group, $n = 3$; experimental group, $n = 3$. WBC, white blood cell; RBC, red blood cell, PLT, platelets; LYM, lymphocytes; Gran, granulocyte; ALT, alanine aminotransferase; AST, aspartate aminotransferase; BUN, blood urea nitrogen; CRE, creatinine.

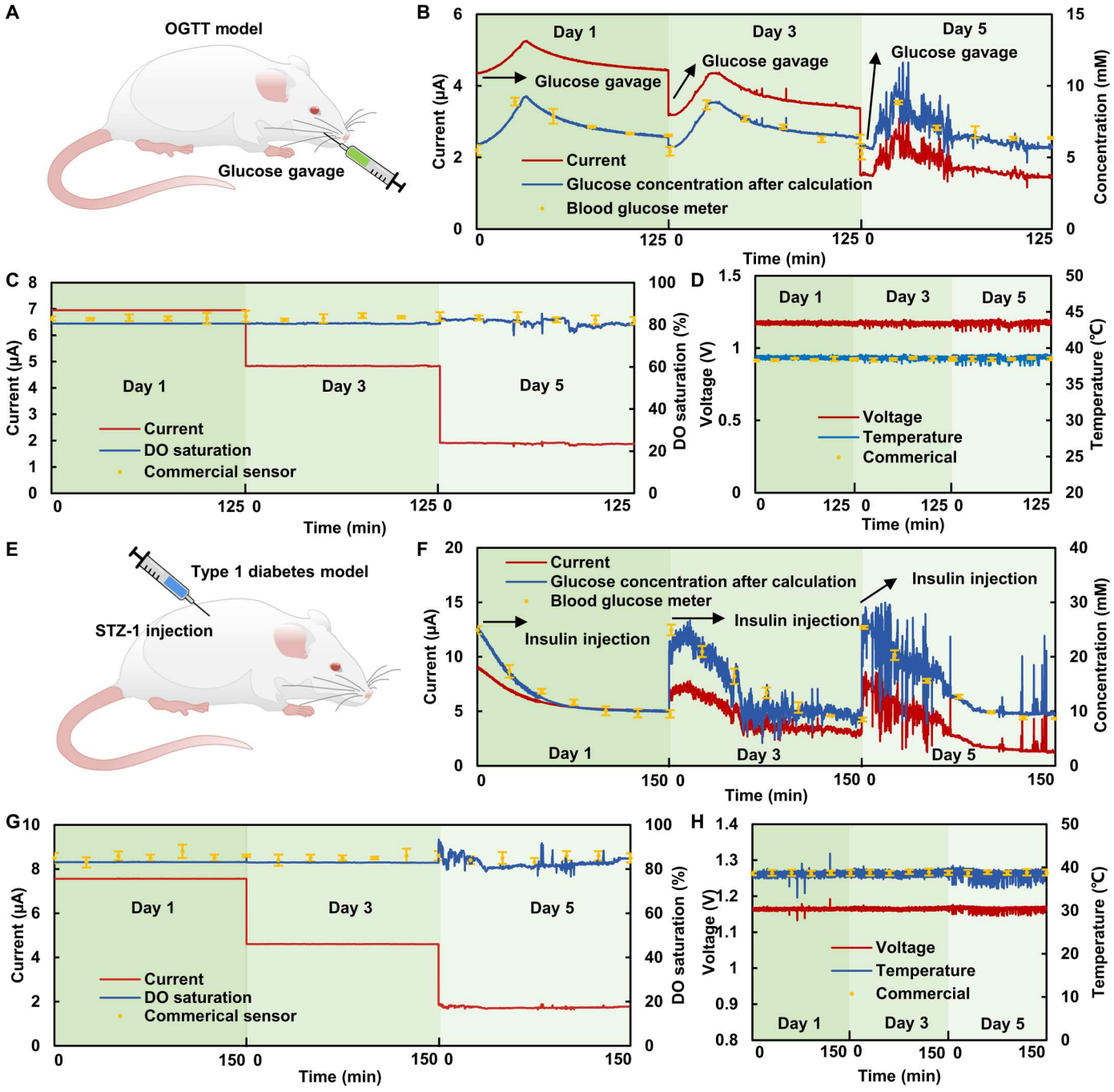

Fig. 5. In vivo evaluations of the bioresorbable electrochemical device. (**A**) Diagram of an OGTT rat who fasted for 24 hours before the experiment followed by instilling 5% glucose solution into the proximal jejunum of the rat on days 1, 3, and 5. Continuous monitoring results of (**B**) glucose, (**C**) DO, and (**D**) temperature obtained on days 1, 3, and 5. Each measurement has been conducted for 125 min each day. (**E**) Diagram of a type 1 diabetic rat who has been injected with 1 U of insulin (physiological saline solution) on days 1, 3, and 5. Continuous monitoring results of (**F**) glucose, (**G**) DO, and (**H**) temperature on days 1, 3, and 5. Each measurement has been conducted for 150 min each day. In (A) and (E), $n = 3$ independent rats.

The bioresorbable electrochemical device was also used to monitor changes in physiological responses before and after insulin injection in type 1 diabetes rats (Fig. 5E). The procedure consisted of two stages, with a rapid decline in current from 9.06 to 5.28 μA during the first 90 min, followed by a gentle drop to a stable value of ~5 μA between 100 and 150 min on the first day (Fig. 5F). Replicate experiments on days 3 and 5 showed similar trends with a decayed current response. Again, the measured DO saturation and the temperature of the rat dorsal subcutaneous tissue can be used to tackle the issue of current drift in the glucose sensor (Fig. 5, G and H), allowing an excellent match between the glucose sensor and the commercial glucometer after

compensation. The in vivo sensing results have demonstrated the capability of the device to work for up to 5 days and the effectiveness in using stable oxygen levels and temperature to compensate for the signal drift and degradation in the glucose sensor.

The noise signals on days 3 and 5 indicate the dissolution of different electrodes in the electrochemical sensor and the dissolution of the outer sensor leads due to wound healing. Day 5 of Fig. 4 (C and D) also demonstrated a slight dissolution of the electrode materials and the outer lead of the sensor. In addition, the stretching and curling of the rat body may cause fluctuations in the collected signals during the measuring process. To meet the requirements of clinical practice, the life span of the bioresorbable electrochemical device can be further improved by adjusting the compositions, molecular weight, and cross-linking levels of the encapsulation and substrate materials. Some surficial corrosion materials such as polycaprolactone, poly(L-lactic acid)–poly(trimethylene carbonate), and polyanhydride may extend the life span of the device to several weeks or even months. This improvement may lead to practical clinical use of the device for long-term implantable applications.

DISCUSSION

This paper has proposed the theories of bioresorbable electrode materials based on galvanic coupling and the corresponding sensing mechanisms, leading to one of the first electrochemical devices that can be fully degraded in a biological environment. The bioresorbable electrochemical device has demonstrated highly specific CGM with a sensing range of 0 to 25 mM, a resolution of 0.1 mM, and a sensitivity of 0.2458 μA/mM. In addition, the self-compensation module consisting of a Zn SE, a temperature sensor, and a DO sensor was also developed to overcome the negative effect due to device degradation. The bioresorbable electrochemical device can maintain stable operation for up to 7 days in vitro and 5 days in vivo and can completely degrade after 8 weeks of implantation without causing apparent inflammation or toxicity. This study may lead to the appearance of more fully bioresorbable and printable implanted devices for chemical detection.

The device and the mechanism presented here are just the first steps toward high-performance bioresorbable electrochemical sensors. With more advanced printing techniques such as aerosol printing and three-dimensional dispersion, it may be feasible to achieve high-precision electrochemical glucose sensors with similar dimensions as the needle-type commercial glucose sensors to match the existing one-press serters that are available in the commercial systems. The miniaturized technology may facilitate the direct implantation of this bioresorbable device by injection through more conventional methods. By properly controlling the number of metals in the sensors, the by-products of the degradation may serve as trace element supplements to offer nutrition or may not generate any negative effect on human health. In addition, the bioresorbable substrates may be modified to integrate specific drugs such as insulin to simultaneously release the drug during the degradation process. Given the effectiveness of the water-sintering method of bioresorbable metallic pastes, it is conceivable the development of more degradable and bioresorbable sensors and actuators integrated with suitable selective membranes, enzymes, and antibodies for in vivo detecting critical biomarkers and conducting closed-loop regulation.

MATERIALS AND METHODS

Preparation of the bioresorbable metal paste

Poly(ethylene oxide) (PEO) powders (molecular weight: 100000; Macklin Shanghai Biochemical Technology Co, Ltd.) were first thoroughly dissolved in dichloromethane (high-performance liquid chromatography, HPLC; Aladin Industrial Corporation) at a weight ratio of 3:97. The resulting solution was further mixed at a weight ratio of 50:25:25 with Mo MPs (average diameter: 1 μm; DK Beijing Technology CO., Ltd) and W MPs (average diameter: 1 μm; DK Beijing Technology CO., Ltd). The mixture was lastly mixed with 4 wt % propionic anhydrides (Aladin Industrial Corporation) to obtain the Mo-W paste. Pure Mo paste and Zn paste were obtained by following a similar procedure as the preparation of the Mo-W paste. The Mo MPs and Zn NPs (average diameter: 50 nm; DK Beijing Technology Co., Ltd) in these pastes have weight ratios of 50 and 50, respectively.

Preparation of the bioresorbable PLGA films

PLGA powders (5 wt %; DG-75DLGH065, Jinan Daigang Biomaterial Co., Ltd) were dissolved in dichloromethane solution through a magnetic stirrer at room temperature. The resulting solution was poured into a Teflon (PTFE, polytetrafluoroethylene) mold and cured at room temperature for 24 hours to obtain PLGA films that can be used either as substrates or encapsulation layers.

Fabrication of the bioresorbable electrochemical device

The temperature sensor and the electrochemical sensors were printed using corresponding metal pastes through a screen printer (PHP-2020A, Hoting Screen Printing Equipment Co., Ltd). The printed patterns can be sintered by applying water droplets through dust-free cotton swabs or using a humidifier that yields more than 90% humidity in a closed chamber to achieve conductive networks. The connection between the bioresorbable electrochemical device and the flexible circuit board was realized by anisotropic conductive film (ACF) (3 M9703, 3 M Company).

Characterization of electrodes

Visualization of MPs and NPs was achieved by an SEM (SUPRA55VP, Carl Zeiss AG). All conductivity measurements were performed by a four-point probe measurement system (ST2253, Crystal Electronics Co., Ltd.) following the ASTM F1711-96 (2008) standard. All electrochemical measurements were conducted using an electrochemical workstation (CHI660E, CH Instrument Inc.). CV tests were carried out at printed electrodes in PBS solution for at least 10 circles until a stable CV curve was obtained. The stability of electrodes with varying composition ratios was investigated using the circuit voltage mode of the electrochemical workstation.

In vitro characterization of the bioresorbable electrochemical device

The fabricated glucose sensor was characterized by immersing it in an electrolyte solution containing 1× PBS solution (pH 7.4; Tianjin Xiqing Jinyuanmao Biological Reagents Business Department) and different concentrations of glucose (Tianjin Jiangtian Huagong Co.) at room temperature. A selectivity study of the glucose sensors was performed by subsequent addition of calcium chloride, sodium chloride, UA, AA, and glucose (2 mM Ca^{2+}, 2 mM Na^{+}, 2 mM

UA, 2 mM AA, and 2 mM glucose) into PBS solution. The fatigue tests were conducted using a tensile tester (HC-01, Dongtai Suheng Transmission Technology Co., Ltd). For the DO sensors, the DO concentration was adjusted by feeding different N_2 and O_2 mixtures in DI water, and a magnetic stirrer was used to ensure better mixing of the solution. The concentration of DO in DI water was measured by a commercial DO probe (JPSJ-605F, INESA Scientific Instruments Co., Ltd). The sensitivity and linearity of the temperature sensor were obtained by placing a sensor on a semiconductor heating sheet (Shanghai Lichen-BX Instrument Technology Co., Ltd.) and measuring its temperature changes from 25° to 50°C.

Biocompatibility tests

Cytotoxicity tests were conducted using the Live/Dead Cell Double Staining Kit and CCK-8 assay by exposing the samples to cultured L-929 cells (Procell Life Science & Technology Co., Ltd.). All sensors were sanitized with 75% alcohol and ultraviolet light, followed by bonding to the bottom of multiwall plates. L-929 cells were then cultured in the plates at 37°C under an atmosphere of 95% air and 5% CO_2. For the Live/Dead Cell Double Staining Kit, cells were dyed by calcein-AM (C1359, Sigma-Aldrich Corp.) and PI (C0080, Solarbio Science & Technology Co., Ltd.) after culturing for 24, 48, and 72 hours, respectively. The fluorescent images were captured by a fluorescence microscope (BX51, Olympus, Corp.). For the CCK-8 assay, each plate was added with 10 μl of CCK-8 solution (CK04, Dojindo Molecular Technologies, Inc.) after culturing the cells for 24, 48, and 72 hours, respectively, followed by incubating for 2 hours. The cytotoxicity was obtained by measuring the absorbance at 450 nm using a microplate photometer (Multiskan FC, Thermo Fisher Scientific Inc.).

In vivo test

All animal studies were conducted at the Tianjin Institute of Radiation Medicine with accreditation number SYXK 2019-0002, under the ethical and operational guidelines mandated by the institute. All the procedures were performed under general anesthesia using isoflurane. Male Lewis rats weighing between 300 and 350 g (Charles River Laboratories) were administered subcutaneous injections of buprenorphine hydrochloride (0.05 mg kg–; Reckitt Benckiser) for pain management and ampicillin (50 mg kg^{-1}; Sage Therapeutics) to prevent infection at the implantation site before the surgical process. The fabricated devices were implanted into the subcutaneous tissue through 5-mm-long incisions on the shaved back of the rats, followed by suturing with surgical sutures. Euthanasia of the rats after 8 weeks of implantation enabled the explanation of organs, including the heart, kidneys, liver, lung, spleen, and skin, as well as the extraction of blood for further biocompatibility studies. For histological analysis, the organs were fixed in formalin (concentration, 10 vol %), followed by embedding in paraffin, sectioning, and staining with H&E. Blood samples collected in K-EDTA and gel tubes were used to prepare samples for complete blood counts and blood chemistry tests.

Supplementary Materials

This PDF file includes:

Supplementary Text
Figs. S1 to S28
Tables S1 to S5

REFERENCES AND NOTES

1. D. Bruen, C. Delaney, L. Florea, D. Diamond, Glucose sensing for diabetes monitoring: Recent developments. *Sensors* **17**, 1866 (2017).
2. D. M. Nathan; DCCT/EDIC Research Group, The diabetes control and complications trial/epidemiology of diabetes interventions and complications study at 30 years: Overview. *Diabetes Care* **37**, 9–16 (2014).
3. X. Xie, J. C. Doloff, V. Yesilyurt, A. Sadraei, J. J. McGarrigle, M. Omami, O. Veiseh, S. Farah, D. Isa, S. Ghani, I. Joshi, A. Vegas, J. Li, W. Wang, A. Bader, H. H. Tam, J. Tao, H.-J. Chen, B. Yang, K. A. Williamson, J. Oberholzer, R. Langer, D. G. Anderson, Reduction of measurement noise in a continuous glucose monitor by coating the sensor with a zwitterionic polymer. *Nat. Biomed. Eng.* **2**, 894–906 (2018).
4. G. Slaughter, T. Kulkarni, Detection of human plasma glucose using a self-powered glucose biosensor. *Energies* **12**, 825 (2019).
5. World Health Organization, "World Health Organization Global Report on Diabetes"ISBN 9789241565257 (World Health Organization, 2016).
6. W. Li, W. Luo, M. Li, L. Chen, L. Chen, H. Guan, M. Yu, The impact of recent developments in electrochemical POC sensor for blood sugar care. *Front Chem.* **9**, 723186 (2021).
7. S. Woderer, N. Henninger, C.-D. Garthe, H. M. Kloetzer, M. Hajnsek, U. Kamecke, N. Gretz, B. Kraenzlin, J. Pill, Continuous glucose monitoring in interstitial fluid using glucose oxidase-based sensor compared to established blood glucose measurement in rats. *Anal. Chim. Acta* **581**, 7–12 (2007).
8. S. Bagyalakshmi, A. Sivakami, K. Balamurugan, A Zno nanorods based enzymatic glucose biosensor by immobilization of glucose oxidase on a chitosan film. *Obes Med.* **18**, 100229 (2020).
9. Z. Pu, X. Zhang, H. Yu, J. Tu, H. Chen, Y. Liu, X. Su, R. Wang, L. Zhang, D. Li, A thermal activated and differential self-calibrated flexible epidermal biomicrofluidic device for wearable accurate blood glucose monitoring. *Sci. Adv.* **7**, eabd0199 (2021).
10. A.-M. Spehar-Délèze, S. Anastasova, P. Vadgama, Monitoring of lactate in interstitial fluid, saliva and sweat by electrochemical biosensor: The uncertainties of biological interpretation. *Chemosensors* **9**, 195 (2021).
11. E. Kemp, T. Palomäki, I. A. Ruuth, Z. A. Boeva, T. A. Nurminen, R. T. Vänskä, L. K. Zschaechner, A. G. Perez, T. A. Hakala, M. Wardale, E. Haeggström, J. Bobacka, Influence of enzyme immobilization and skin-sensor interface on non-invasive glucose determination from interstitial fluid obtained by magnetohydrodynamic extraction. *Biosens. Bioelectron* **206**, 114123 (2022).
12. M. Mohammadifar, M. Tahernia, S. Choi, An equipment-free, paper-based electrochemical sensor for visual monitoring of glucose levels in urine. *SLAS Technol.* **24**, 499–505 (2019).
13. M. F. Hossain, J. Y. Park, Plain to point network reduced graphene oxide-activated carbon composites decorated with platinum nanoparticles for urine glucose detection. *Sci. Rep.* **6**, 21009 (2016).
14. E. V. Karpova, E. V. Shcherbacheva, A. A. Galushin, D. V. Vokhmyanina, E. E. Karyakina, A. Karyakin, Noninvasive diabetes monitoring through continuous analysis of sweat using flow-through glucose biosensor. *Anal. Chem.* **91**, 3778–3783 (2019).
15. G. Fabregat, S. Lanzalaco, J. A. Saïd, X. Muñoz-Pascual, J. Llorca, C. Alemán, Immobilization of glucose oxidase on plasma-treated polyethylene for non-invasive glucose detection. *J. Electroanal. Chem.* **895**, 115509 (2021).
16. C. Gorst, C. S. Kwok, S. Aslam, I. Buchan, E. Kontopantelis, P. K. Myint, G. Heatlie, Y. Loke, M. K. Rutter, M. Mamas, Long-term glycemic variability and risk of adverse outcomes: A systematic review and meta-analysis. *Diabetes Care* **38**, 2354–2369 (2015).
17. A. L. Carlson, D. M. Mullen, R. M. Bergenstal, Clinical use of continuous glucose monitoring in adults with type 2 diabetes. *Diabetes Technol. Ther.* **19**, S4–S11 (2017).
18. P. Prahalad, A. Addala, D. Scheinker, K. K. Hood, D. M. Maahs, CGM initiation soon after type 1 diabetes diagnosis results in sustained CGM use and wear time. *Diabetes Care* **43**, e3–e4 (2020).
19. S.-K. Kang, R. K. J. Murphy, S.-W. Hwang, S. M. Lee, D. V. Harburg, N. A. Krueger, J. Shin, P. Gamble, H. Cheng, S. Yu, Z. Liu, J. G. McCall, M. Stephen, H. Ying, J. Kim, G. Park, R. C. Webb, C. H. Lee, S. Chung, D. S. Wie, A. D. Gujar, B. Vemulapalli, A. H. Kim, K.-M. Lee, J. Cheng, Y. Huang, S. H. Lee, P. V. Braun, W. Z. Ray, J. A. Rogers, Bioresorbable silicon electronic sensors for the brain. *Nature* **530**, 71–76 (2016).
20. C. M. Boutry, Y. Kaizawa, B. C. Schroeder, A. Chortos, A. Legrand, Z. Wang, J. Chang, P. Fox, Z. Bao, A stretchable and biodegradable strain and pressure sensor for orthopaedic application. *Nat. Electron.* **1**, 314–321 (2018).
21. Y. S. Choi, Y.-Y. Hsueh, J. Koo, Q. Yang, R. Avila, B. Hu, Z. Xie, G. Lee, Z. Ning, C. Liu, Y. Xu, Y. J. Lee, W. Zhao, J. Fang, Y. Deng, S. M. Lee, A. Vázquez-Guardado, I. Stepien, Y. Yan, J. W. Song, C. Haney, Y. S. Oh, W. Liu, H.-J. Yoon, A. Banks, M. R. Mac Ewan, G. A. Ameer, W. Z. Ray, Y. Huang, T. Xie, C. K. Franz, S. Li, J. A. Rogers, Stretchable, dynamic covalent polymers for soft, long-lived bioresorbable electronic stimulators designed to facilitate neuromuscular regeneration. *Nat. Commun.* **11**, 5990 (2020).

22. G. Yao, L. Kang, C. Li, S. Chen, Q. Wang, J. Yang, Y. Long, J. Li, K. Zhao, W. Xu, W. Cai, Y. Lin, X. Wang, A self-powered implantable and bioresorbable electrostimulation device for biofeedback bone fracture healing. *Proc. Natl. Acad. Sci. U.S.A.* **118**, e2100772118 (2021).
23. G. Lee, E. Ray, H.-J. Yoon, S. Genovese, Y. S. Choi, M.-K. Lee, S. Şahin, Y. Yan, H.-Y. Ahn, A. J. Bandodkar, J. Kim, M. Park, H. Ryu, S. S. Kwak, Y. H. Jung, A. Odabas, U. Khandpur, W. Z. Ray, M. R. MacEwan, J. A. Rogers, A bioresorbable peripheral nerve stimulator for electronic pain block. *Sci. Adv.* **8**, eabp9169 (2022).
24. R. Li, H. Qi, Y. Ma, Y. Deng, S. Liu, Y. Jie, J. Jing, J. He, X. Zhang, L. Wheatley, C. Huang, X. Sheng, M. Zhang, L. Yin, A flexible and physically transient electrochemical sensor for real-time wireless nitric oxide monitoring. *Nat. Commun.* **11**, 3207 (2020).
25. E. Bihar, S. Wustoni, A. M. Pappa, K. N. Salama, D. Baran, S. Inal, A fully inkjet-printed disposable glucose sensor on paper. *npj Flex. Electron.* **2**, 30 (2018).
26. S. M. Yang, J. H. Shim, H.-U. Cho, T.-M. Jang, G.-J. Ko, J. Shim, T. H. Kim, J. Zhu, S. Park, Y. S. Kim, S.-Y. Joung, J. C. Choe, J.-W. Shin, J. H. Lee, Y. M. Kang, H. Cheng, Y. Jung, C.-H. Lee, D. P. Jang, S.-W. Hwang, Hetero-integration of silicon nanomembranes with 2D materials for bioresorbable, wireless neurochemical system. *Adv. Matter.* **34**, 2108203 (2022).
27. D. Jones, Principles and prevention. 2, 168 (1996).
28. L. A. Pawlick, G. E. Stoner, G. G. Clemeña, "Development of an embeddable reference electrode for reinforced concrete structures" (Technical Report VTRC 99-CR1, Virginia Transportation Research Council, 1998).
29. R. C. Dawkins, D. Wen, J. N. Hart, M. Vepsäläinen, A screen-printed Ag/AgCl reference electrode with long-term stability for electroanalytical applications. *Electrochim. Acta* **393**, 139043 (2021).
30. G.-R. Li, X.-P. Gao, Low-cost counter-electrode materials for dye-sensitized and perovskite solar cells. *Adv. Mater.* **32**, 1806478 (2020).
31. L. Wang, G.-R. Li, Q. Zhao, X.-P. Gao, Non-precious transition metals as counter electrode of perovskite solar cells. *Energy Stor. Mater.* **7**, 40–47 (2017).
32. R. Feng, Y. Chu, X. Wang, Q. Wu, F. Tang, A long-term stable and flexible glucose sensor coated with poly (ethylene glycol)-modified polyurethane. *J. Electroanal. Chem.* **895**, 115518 (2021).
33. J. Soto, T. Hughes, Y. S. Li, Silicon-based glucose oxidase working electrode for glucose sensing. *ACS Omega* **4**, 18312–18316 (2019).
34. Y. Cheng, X. Gong, J. Yang, G. Zheng, Y. Zheng, Y. Li, Y. Xu, G. Nie, X. Xie, M. Chen, C. Yi, L. Jiang, A touch-actuated glucose sensor fully integrated with microneedle array and reverse iontophoresis for diabetes monitoring. *Biosens. Bioelectron.* **203**, 114026 (2022).
35. G. Valdés-Ramírez, Y.-C. Li, J. Kim, W. Jia, A. J. Bandodkar, R. Nuñez-Flores, P. R. Miller, S.-Y. Wu, R. Narayan, J. R. Windmiller, R. Polsky, J. Wang, Microneedle-based self-powered glucose sensor. *Electrochem. Commun.* **47**, 58–62 (2014).
36. Y. Liu, Q. Yu, X. Luo, L. Yang, Y. Cui, Continuous monitoring of diabetes with an integrated microneedle biosensing device through 3D printing. *Microsyst. Nanoeng.* **7**, 75 (2021).
37. F. Ribet, G. Stemme, N. Roxhed, Real-time intradermal continuous glucose monitoring using a minimally invasive microneedle-based system. *Biomed. Microdevices* **20**, 101 (2018).
38. K. B. Kim, H. Choi, H. J. Jung, Y.-J. Oh, C.-H. Cho, J. H. Min, S. Yoon, J. Kim, S. J. Cho, H. J. Cha, Mussel-inspired enzyme immobilization and dual real-time compensation algorithms for durable and accurate continuous glucose monitoring. *Biosens. Bioelectron.* **143**, 111622 (2019).
39. I. Shitanda, K. Oda, N. Loew, H. Watanabe, M. Itagaki, S. Tsujimura, A. Zebda, Chitosan-based enzyme ink for screen-printed bioanodes. *RSC Adv.* **11**, 20550–20556 (2021).
40. S.-J. Li, N. Xia, X.-L. Lv, M.-M. Zhao, B.-Q. Yuan, H. Pang, A facile one-step electrochemical synthesis of graphene/NiO nanocomposites as efficient electrocatalyst for glucose and methanol. *Sens. Actuators B Chem.* **190**, 809–817 (2014).
41. A. Abellán-Llobregat, I. Jeerapan, A. Bandodkar, L. Vidal, A. Canals, J. Wang, E. Morallon, A stretchable and screen-printed electrochemical sensor for glucose determination in human perspiration. *Biosens. Bioelectron.* **91**, 885–891 (2017).
42. M. Awad, B. Al-Jahdaly, O. A. Hazazi, M. A. Kassem, Cobalt and nickel nanoparticles binary catalyst modified glassy carbon electrode for glucose and ascorbic acid electrooxidation in alkaline medium. *Int. J. Electrochem. Sci.* **16**, 150486 (2021).
43. Y. H. Yun, B. K. Lee, J. S. Choi, S. Kim, B. Yoo, Y. S. Kim, K. Park, Y. W. Cho, A glucose sensor fabricated by piezoelectric inkjet printing of conducting polymers and bienzymes. *Anal. Sci.* **27**, 375–379 (2011).
44. M. A. Zahed, S. C. Barman, P. S. Das, M. Sharifuzzaman, H. S. Yoon, S. H. Yoon, J. Y. Park, Highly flexible and conductive poly (3, 4-ethylene dioxythiophene)-poly (styrene sulfonate) anchored 3-dimensional porous graphene network-based electrochemical biosensor for glucose and pH detection in human perspiration. *Biosens. Bioelectron.* **160**, 112220 (2020).
45. M. Parrilla, U. Detamornrat, J. Domínguez-Robles, R. F. Donnelly, K. De Wael, Wearable hollow microneedle sensing patches for the transdermal electrochemical monitoring of glucose. *Talanta* **249**, 123695 (2022).
46. K. B. Kim, W.-C. Lee, C.-H. Cho, D.-S. Park, S. J. Cho, Y.-B. Shim, Continuous glucose monitoring using a microneedle array sensor coupled with a wireless signal transmitter. *Sens. Actuators B Chem.* **281**, 14–21 (2019).
47. Y. Cai, B. Liang, S. Chen, Q. Zhu, T. Tu, K. Wu, Q. Cao, L. Fang, X. Liang, X. Ye, One-step modification of nano-polyaniline/glucose oxidase on double-side printed flexible electrode for continuous glucose monitoring: Characterization, cytotoxicity evaluation and in vivo experiment. *Biosens. Bioelectron.* **165**, 112408 (2020).
48. M. Dervisevic, M. Alba, L. Yan, M. Senel, T. R. Gengenbach, B. Prieto-Simon, N. H. Voelcker, Transdermal electrochemical monitoring of glucose via high-density silicon microneedle array patch. *Adv. Funct. Matter.* **32**, 2009850 (2022).

Acknowledgments

Funding: This work was supported by the National Natural Science Foundation of China under grant no. 52121002, the Key Research and Development Program of Zhejiang Province under no. 2022C04004, and the Beijing Natural Science Fund under grant no. Z220015. X.H. would like to thank the support from the Natural Science Foundation of Tianjin under grant no. 21JCQNJC00680. **Author contributions:** Conceptualization: J. Li. and X.H. Methodology: J. Li, J. Liu, and X.H. Investigation: J. Li, J. Liu, and X.H. Visualization: J. Li, J. Liu, Z.W., X.S., and Y.L. Supervision: J. Li, W.H., and X.H. Writing—original draft: J. Li and X.H. Writing—review and editing: J. Li and X.H. **Competing interests:** The authors declare that they have no competing interests. **Data and materials availability:** All data needed to evaluate the conclusions in the paper are present in the paper and/or the Supplementary Materials.

Submitted 22 April 2023
Accepted 16 June 2023
Published 19 July 2023
10.1126/sciadv.adi3839